Chapter 3

BLDC Motor Drive with Adaptable Multifunction Power Processor Having Multimode Operations

3.1 Introduction

This chapter presents a BLDC motor drive with an adaptable multifunction power processor having multimode operations. In multifunction operation, the proposed power processor performs charging as well as motoring operations. In charging mode, it charges the battery from a single-phase AC supply and maintains the unity power factor at the source terminal. In motoring operation, the multifunction power processor drives the brushless DC (BLDC) motor with High pulse width modulation, low-ON (HPLN) switching technique. In multimode operation, the power processor restructured itself and provides vehicle-to-vehicle charging. In all the operations, the auxiliary power supplies are available to power the EV cabin.

Conventionally, two separate converters are used for charging and driving operations. An additional unidirectional DC-DC converter charges the 12 V auxiliary battery, which powers the low-power auxiliaries, such as the music system, lock, and wiper. Furthermore, a bidirectional DC-DC converter is used for vehicle-to-vehicle charging. All these different converters for multifunction and multimode operation increase the cost and weight of the EVs.

The proposed converter performs the single-phase charging, BLDC motor driving, V2V charging, and powering the auxiliaries of the EV cabin through a single converter. Thus, it eliminates the requirement for separate converters, resulting in improved power density. In charging mode, a front-end converter with the field winding of the BLDC motor integrated with a resonant converter that charges the battery with CC-CV charging, along with maintaining the unity power factor at the source terminal. In motoring mode, the front-end converter and resonant converter reconfigure themselves to drive the BLDC motor with HPLN switching. Further, for V2V charging, it reconfigured itself with three changeover switches. During these operations, the regulated multioutputs is available for the EV cabin.

All these operations are mutually exclusive. Therefore, the mode transformation takes place with the help of seven changeover switches under standstill conditions. The operation of the proposed converter can be understood by the block diagram of the proposed system, as shown in Fig.3. 1.

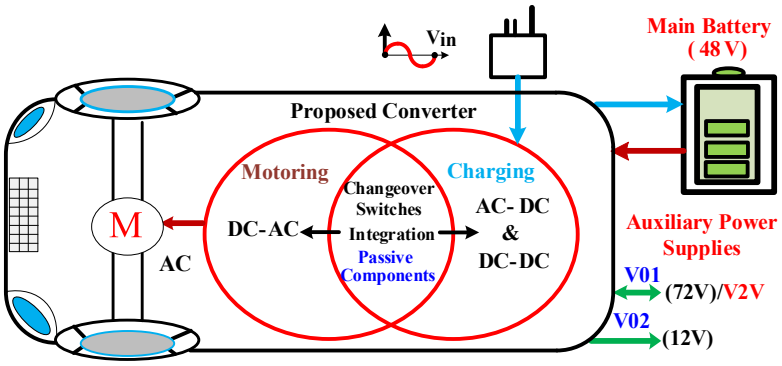

Fig.3. 1 Block diagram of a BLDC motor drive with an adaptable multifunction power processor having multimode operations.

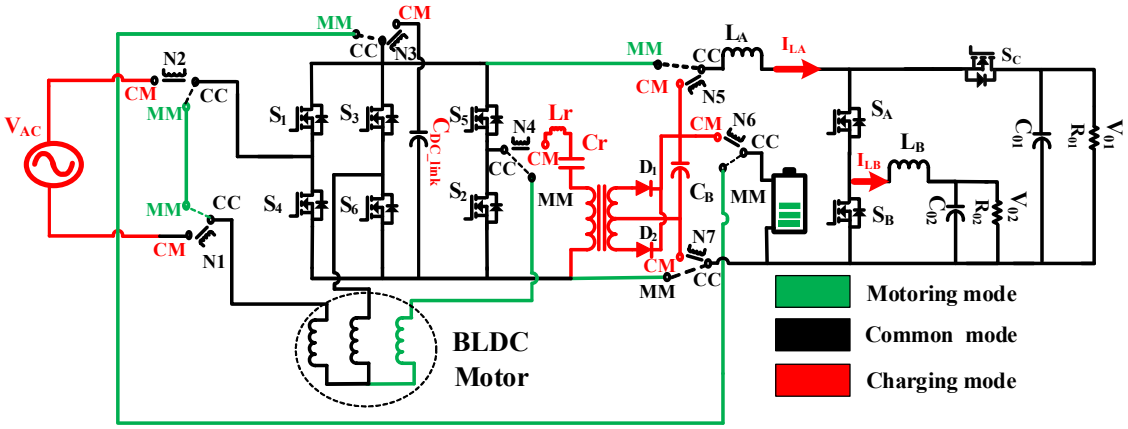

Fig.3. 2 Circuit diagram of a BLDC motor drive with an adaptable multifunction power processor having multimode operations.

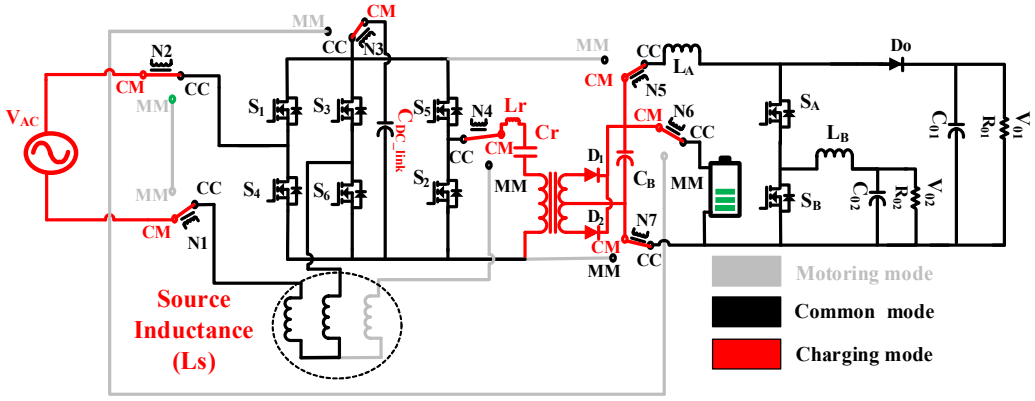

Fig.3. 3 Circuit diagram of the proposed power processor in charging mode.

3.2 Multifunction operation of the proposed converter

The proposed on-board charger allows the use of a single converter to operate both in charging as well as motoring modes with the help of the changeover switches, as shown in Fig.3. 2. Each of the additional switches has three contact points: 1) Common connector mode

(CC), 2) Charging connector mode (CM), and 3) Motoring connector mode (MM). When the changeover switches are energized, the CC-CM contacts of the switches are connected to form the charging mode, as shown in Fig.3. 3, and when relays are de-energized, the CC-MM contactors of the relays form the motoring mode, as shown in Fig.3. 4.

3.2.1 Motoring mode operation of the proposed power converter

In motoring mode, the changeover switches are de-energized to form the CC-MM connection of the switches, as shown in Fig.3. 4, which consists of an inverter with auxiliary power supplies.

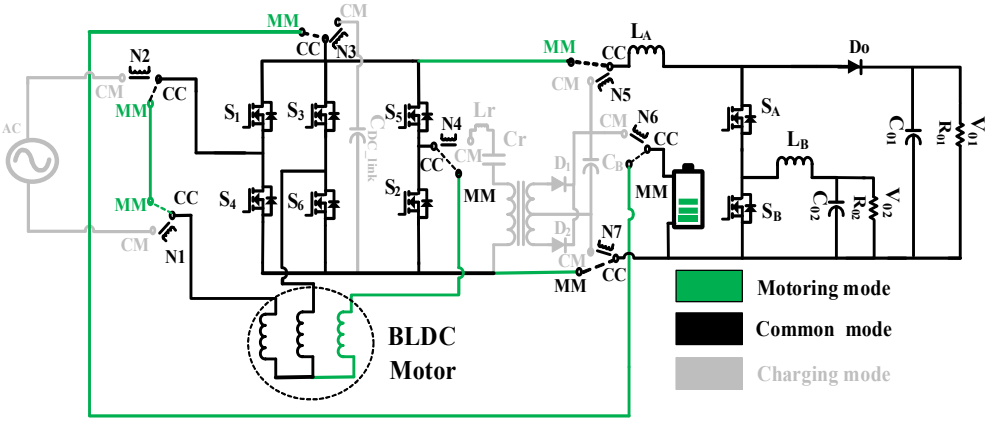

Fig.3. 4 Circuit diagram of the proposed power processor in motoring mode.

3.2.1.1 Appearance of the inverter in motoring mode

The inverter has appeared from the front-end converter and the resonant converter of the charging mode with the help of relays N1-N4. The auxiliary power supplier is integrated with motoring mode with the help of relays N5 and N7. The inverter is used to drive the BLDC motor. The BLDC motor has two operating states: conduction and commutation [97], [98]. In the conduction state, two phases of the inverter conduct, depending on the rotor position. Further, the commutation state is a transition period in which one switch from the two conducting phases is turned OFF, and the next switch of the third phase is turned ON, depending on the rotor position. According to this operating cycle, the BLDC motor stator winding operating with the conventionally used six-step switching has two types of current ripples (or torque ripples):1) The conduction current ripples and 2) The commutation current ripples.

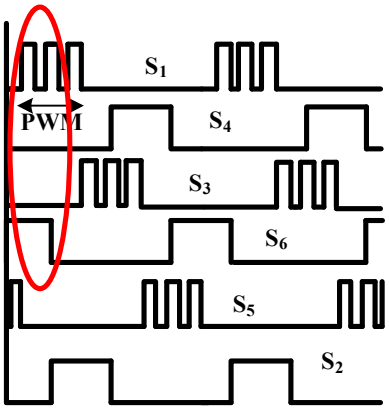

Fig.3. 5 HPLN switching scheme.

3.2.1.2 Commutation torque ripple minimization

The minimisation of commutation current ripples is achieved by implementing the HPLN switching scheme, as shown in Fig.3. 5, and according to this switching scheme, the operation of the proposed system in motoring mode is shown in Fig.3. 6. Fig.3. 6 (a) and (b) show the different switching states of converter operation to implement the HPLS scheme. At the time when switches S_1 and S_6 are turned ON, the converter switching state is shown in Fig.3. 6 (a).

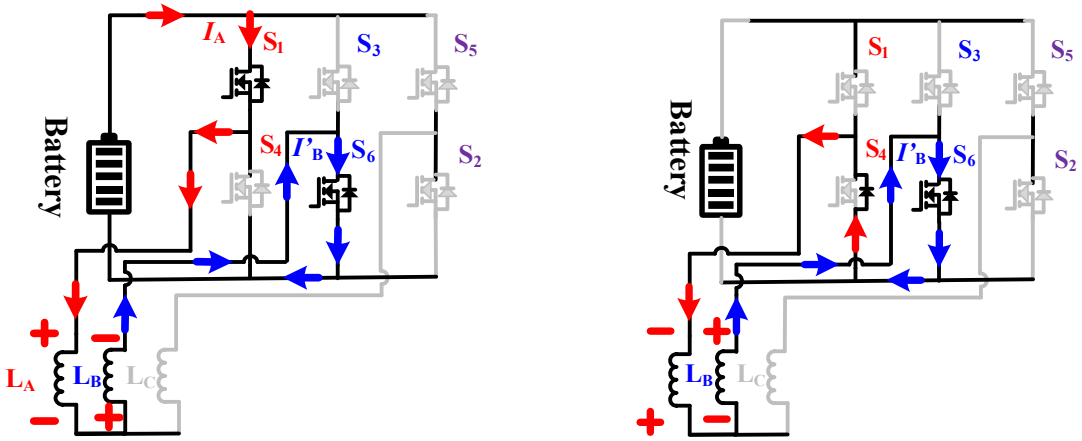

(a) (b)

Fig.3. 6 Inverter operation in the high-frequency switching during of switch S_1, (a) inverter operation when switches S_1 is being turned on, and S_6 is already conducting, and (b) free-wheeling period of the inverter when switch S_1 is turned OFF while S_6 is already conducting.

The power is delivered from the DC source to the load through the interaction of the stator and the rotor magnetic fields. When switch S_1 is turned OFF and switch S_6 remains ON, the free-wheeling operation occurs through the complementary switch anti-parallel diode, as shown in Fig.3. 6(b) Due to this free-wheeling operation, the stator winding releases its energy completely through the same inverter leg.

Table 3. 1 Six-step High-PWM Low-ON switching for BLDC motor drive

Position of PM magnet axis	Output of Hall effect sensors			Phase A		Phase B		Phase C	
	H_1	H_2	H_3	S_1	S_4	S_3	S_6	S_5	S_2
$330^0< \theta \leq 30^0$	0	0	1	0	0	0	ON	PWM	0
$30^0< \theta \leq 90^0$	1	0	1	PWM	0	0	ON	0	0
$90^0< \theta \leq 150^0$	1	0	0	PWM	0	0	0	0	ON
$150^0< \theta \leq 210^0$	1	1	0	0	0	PWM	0	0	ON
$210^0< \theta \leq 270^0$	0	1	0	0	ON	PWM	0	0	0
$270^0< \theta \leq 330^0$	0	1	1	0	ON	0	0	PWM	0

In this way, during the commutation period (switch S_1 is OFF and switch S_3 is turned ON), the commutation current ripple is greatly reduced from the lower switches of inverters S_4. In a similar way, the commutation current ripple is reduced from the commutation current of switches S_6 and S_2. The switching operation of the inverter is done as given in the look-up Table 3. 1 The inverter switches S_1, S_3, and S_5 are triggered with a PWM switching scheme for controlling the speed and reducing the commutation torque ripple of the motor, and the switches S_4, S_6, and S_2 are ON in their respective time interval according to the lookup table.

3.2.2 Charging mode operation

In the charging mode, the changeover switches are energized, and relays form the CC-CM connection, as shown in Fig.3. 3. The charging mode of the integrated converter consists of a front-end converter, a resonant converter, and an auxiliary power supply circuit.

3.2.2.1 Front-end converter of charging mode (FEC)

In the charging mode, FEC is transformed from the inverter switches S_1, S_3, S_4, and S_6, with the help of the changeover switches N1 and N2. The DC-link capacitor is connected to the FEC with the help of the changeover switch N3. During the charging mode operation, the stator winding of a three-phase BLDC motor is used as the source inductor of the front-end converter. It is to be noted that the hall effect sensors that determine the rotor position of the BLDC motor are not turned on. Since the sensors do not provide any output, no PWM signals will be generated for the electronic commutation of the BLDC motor. This prevents any rotation of the motor in charging mode. The motor will not be rotated with the 1-phase AC supply, and this can be understood by the working principle of the BLDC motor.

A single-phase AC supply is applied to the boost power factor correction (PFC) front-end converter to charge the battery, as shown in Fig.3. 7. The single-phase AC supply has a frequency of 50 Hz, and the FEC converter is switching at 20 k Hz.

FEC operation during the positive cycle of the AC source is shown in Fig.3. 7. In this duration, either the switch S_4 S_6 is ON or OFF, and the direction of the current in the stator winding inductor La, Lb of phases a & b of the BLDC motor remains the same, as shown in

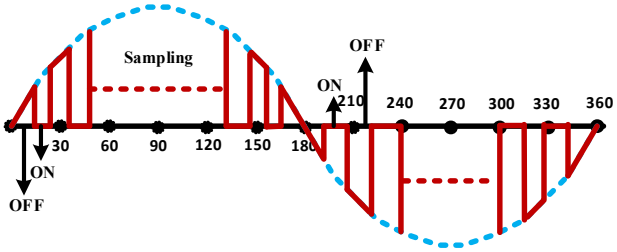

Fig.3. 7 Switching sequence for FEC during charging mode.

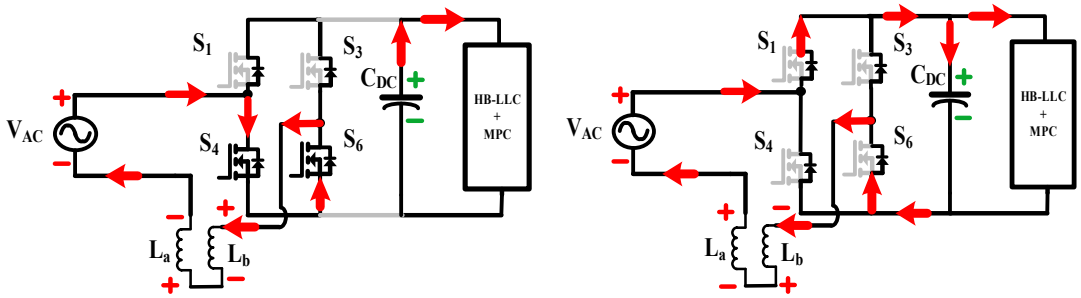

Fig.3. 8 Switching sequence for the positive cycle of supply source, (a) when switches S_4, and S_6 are ON, (b) when switches S_4, and S_6 are OFF.

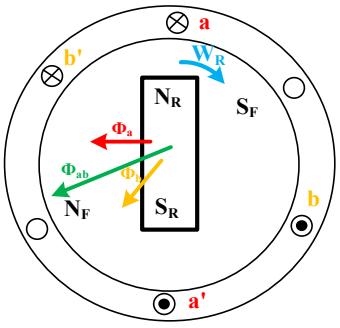

Fig.3. 9 The reaction of the BLDC motor during switching in positive cycle of supply source.

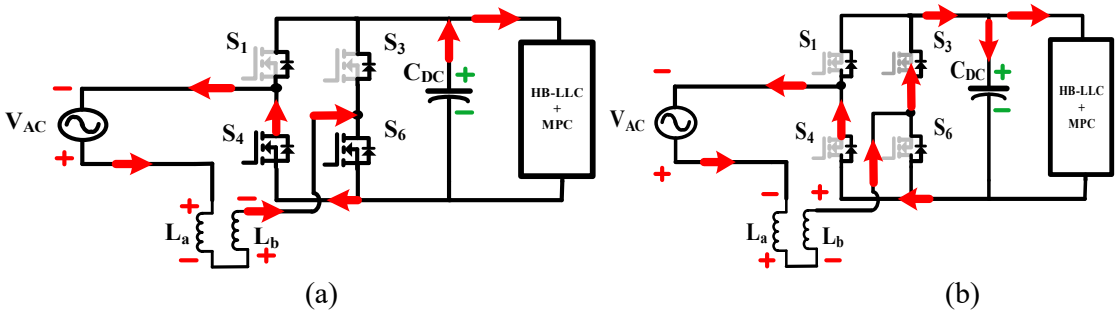

Fig.3. 10 Switching sequence for the negative cycle of supply source, (a) when switches S_4, and S_6 are ON, (b) when switches S_4, and S_6 are OFF.

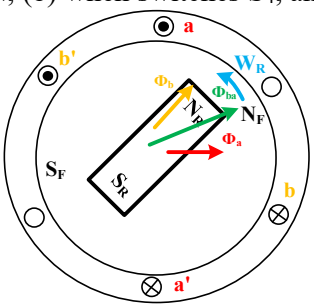

Fig.3. 11 The reaction of the BLDC motor during switching in negative cycle of supply source.

Fig.3. 8 (a) and (b), respectively. The inductors L_a and L_b are the stator winding of the BLDC motor. According to that current, the behaviour of the BLDC motor is shown in Fig.3. 9. When the current enters through phase-A and leaves through phase-B, then according to Maxwell's right-hand thumb rule, the magnetic field direction is given in Fig.3. 9. The magnetic field by the current I_a is represented by Φ_a, and the magnetic field by the current I_b is represented by Φ_b. The resultant magnetic field by the phase-ab is represented by Φ_{ab}. Inside the magnet, the magnetic field line goes through S to N pole, and outside of the magnet, the magnetic field line goes through N to S. So, according to the outer side of the magnet, the magnetic poles N_F and S_F are induced by the magnetic field Φ_{ab}. The permanent magnet N_R -S_R poles are attracted by the filed poles N_F - S_F. This attraction pushes the permanent magnet rotor in a clock direction.

FEC operation during the negative cycle of the AC supply source is shown in Fig.3. 10. In this duration, either the switch S_4 S_6 is ON or OFF, and the direction of the current in the stator winding inductors L_a, L_b of phases a & b of the BLDC motor remains the same, as shown in Fig.3. 10 (a) and (b), respectively. According to the current, the behaviour of the BLDC motor is shown in Fig.3. 11. The permanent magnet N_R -S_R poles ripple by the field poles N_F - S_F. This repulsion pushes the permanent magnet rotor in an anti-clockwise direction. Therefore, the rotor remains stationary during the charging operation.

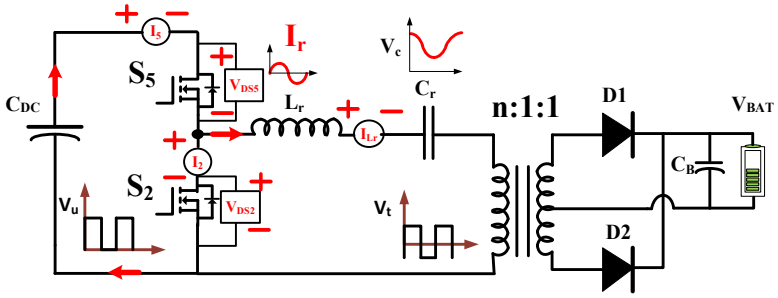

Fig.3. 12 Circuit diagram of HB-LLC converter.

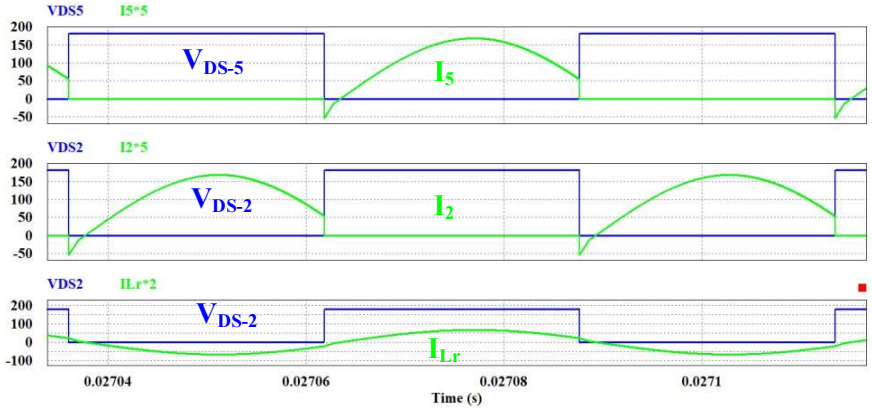

Fig.3. 13 Simulation result of the ZVS condition of HB-LLC switches S5 and S2.

3.2.2.2 Resonant part of the proposed converter (HB-LLC)

Zero voltage switching (ZVS) is a very important technique for reducing switching losses in any converter. In the ZVS technique, the current should lag behind the voltage across the switch. During the transition time of the switch from OFF to ON, the lagging current should flow through the anti-parallel diode. The current and voltage direction of HB-LLC is considered according to Fig.3. 12. The simulation results in Fig.3. 13 represent the ZVS condition of switches S_5 and S_2 of the HB-LLC converter when the switch is ON, current flows through the body diode of the switch.

Gain of the HB-LLC Converter

The normalized value of voltage gain Mg_n, and the battery terminal voltage V_{bat} of the HB-LLC can be expressed as

$$Mg_n = \left| \frac{L_n * {f_n}^2}{[(L_n+1)*{f_n}^2-1]+j[({f_n}^2-1)*f_n*Q_L*L_n]} \right| \tag{3.1}$$

$$V_{bat} = Mg_{n*}\frac{1}{n} * \frac{V_{DC\_Link}}{2} \tag{3.2}$$

Where: f_n is the normalized frequency, L_n is the inductance ratio of the magnetizing inductance and leakage inductance (L_m/L_r), and Q_L is the quality factor.

To achieve a unity gain, the HB-LLC converter is switched at its normalized frequency ($f_n = \frac{f_{switching}}{f_{resonance}}$). The unity gain is invariant with respect to the quality factor and the inductance ratio of the converter.

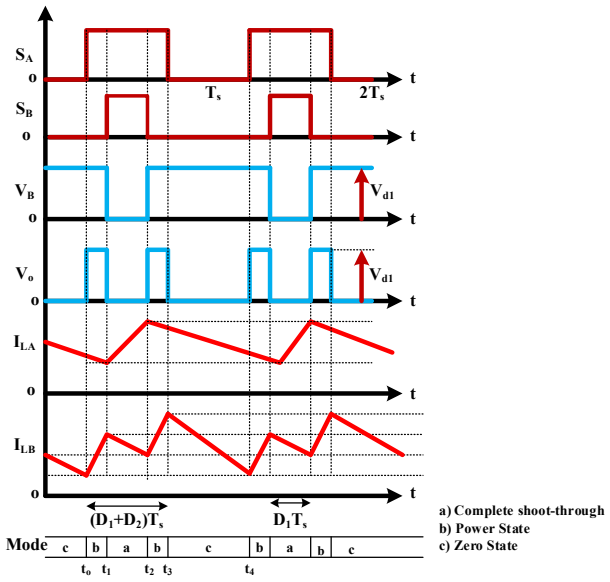

Fig.3. 14 Proposed converter operation for auxiliary power supply.

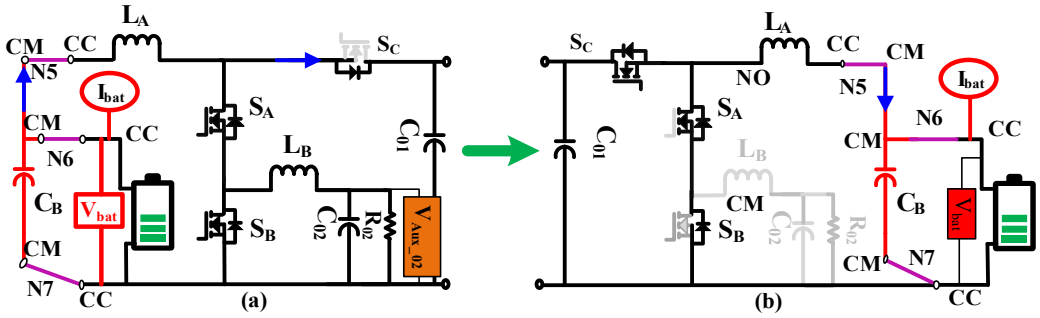

Fig.3. 15 Circuit used for V2V charging, (a) circuit of energy supplier vehicle, and (b) circuit of energy acceptor vehicle.

3.2.3 V2V charging with auxiliary power supply

The operation of the auxiliary power supply through the proposed converter can be understood by its switching sequence, as shown in Fig.3. 14. According to the switching sequence, the operation of the converter can be divided into three parts; a) complete shoot-through (D_1) (S_A and S_B both switch is ON), b) Power state (D_2) (S_A remains ON and S_B OFF),

and c) Zero state (S_A and S_B are OFF). During complete shoot-through intervals, energy is stored in the inductor L_A, and stored energy is released in load R_{01} in the power state and loads R_{01} and R_{02} in the zero state. However, in inductor L_B, energy is stored in the power state, and the stored energy is released in a complete shoot-through and zero state in load R_{02}.

The auxiliaries' power supply is generated in charging as well as in motoring mode of operation, with different orientations of relays N5, N6, and N7, as shown in Fig.3. 15 (a). In its charging mode, it takes power from the input AC supply source, and in its motoring mode, it takes power from the battery source to generate a boost and buck voltage for powering up the EV cabin. For V2V charging, the 72 V boost output of the power converter is used as a connecting point between the proposed power converter for energy exchange. The supplier and acceptor vehicle circuit diagram of the proposed power converter is shown in Fig.3. 15 (a) and (b), respectively.

3.2.3.1 Steady-state relation between auxiliary power supply

By applying the flux balance in inductors L_A and L_B, the steady state voltage equation of the boost and buck values of the auxiliary power supplies is given by:

$$V_{01} = \frac{V_{bat}}{(1-D_1)} \tag{3.3}$$

$$V_{02} = V_{01} * D_2 \tag{3.4}$$

3.3 Control of the multifunction proposed power converter

3.3.1 Motoring mode control

The control logic for the motoring mode is shown in Fig.3. 16. In motoring mode, the speed of the motor and the regulated auxiliary power supply are controlled. Two main methods control the speed of the BLDC motor: 1) Voltage control and 2) PWM control. In voltage control, the speed of the BLDC is directly proportional to the applied voltage. While in the PWM control scheme, the speed of the motor is controlled by the duty cycle of the applied PWM. Higher turn-on time increases the average voltage, increasing the speed of the motor. Further, for the decrease in speed, decrease the turn-on time of the PWM. The control algorithm for the speed control of the BLDC motor in the proposed system is shown in Fig.3. 16(a). The High PWM switching in S_1, S_3, and S_5 of the upper leg of the inverter changes the average applied voltage to the motor. The lower switches S_4, S_6, and S_2 are turned on in their respective time intervals.

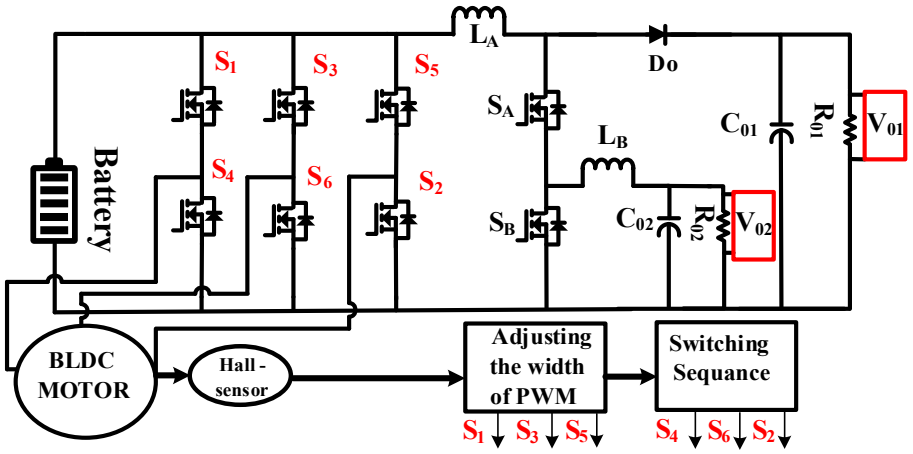

(a)

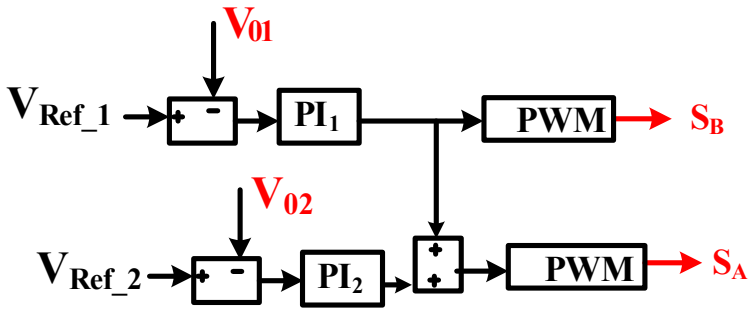

(b)

Fig.3. 16 (a) Control technique of the BLDC motor speed control, and (b) control technique for auxiliary power supply.

In motoring mode, along with the speed of the motor, the regulated auxiliary power supply is also controlled for the EV cabin. The controlled logic for the auxiliary power supply is given in Fig.3. 16(b). The boost output (72 V) is compared to the set value and sent to the PI controller (PI_1). The PWM pulse generated using the output of the PI controller is triggered to the switch S_B. The buck output (12 V) of the converter is compared to the set value, and the error is minimized by another PI controller (PI_2) and added to the output of the PI_1 controller. The generated pulse is triggered by the switch S_A, with the help of these PI controllers. The regulated auxiliary power supply of 12 V and 72 V maintains the cabin in the EV.

3.3.2 Charging mode control

In the charging mode, the controller maintains a unity power factor at the source terminal and charges the battery with the CC-CV charging algorithm, along with maintaining the auxiliary power of the cabin of EVs [99], [100]. The unified control loop technique of the

charging mode is shown in Fig.3. 19. The stepwise operation of the unified control loop is given in the following subsections.

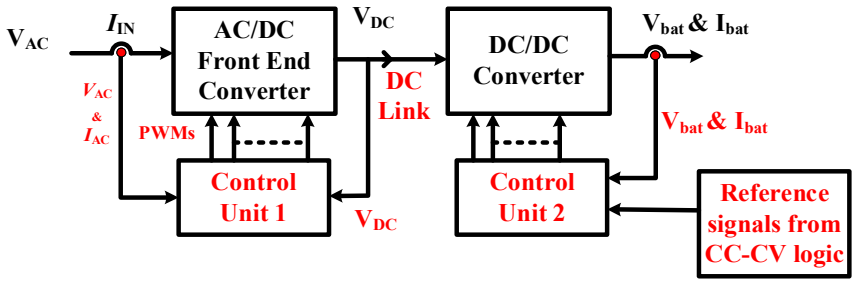

Fig.3. 17 Conventional two-stage controller for EV charging.

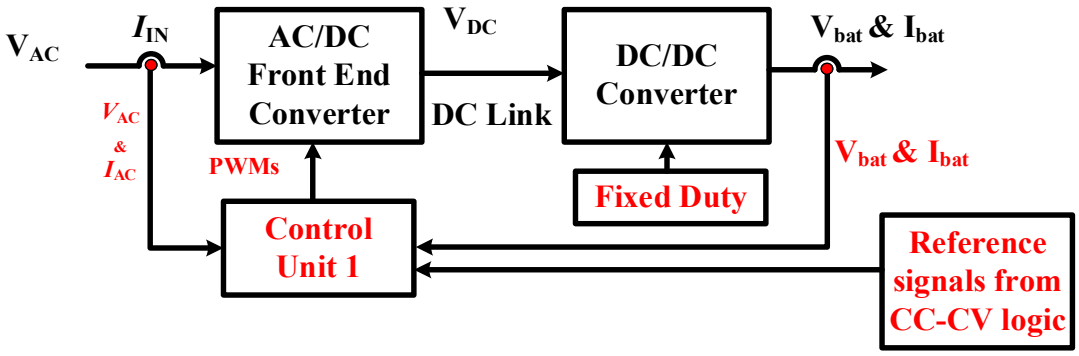

Fig.3. 18 Single-stage controller for EV charging.

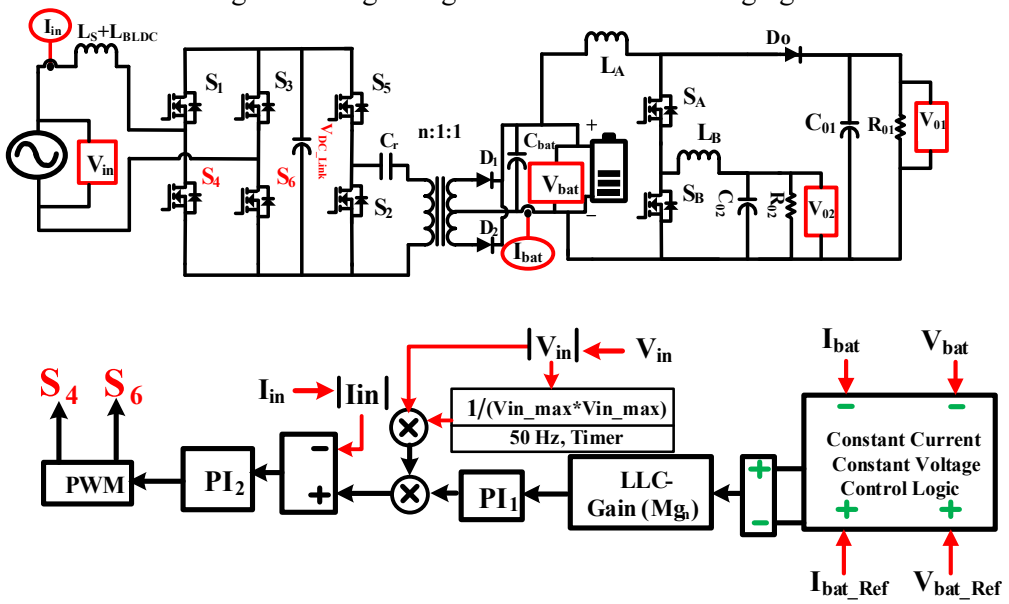

Fig.3. 19 Charging mode control of the proposed multimode on-board power converter.

3.3.2.1 Single-loop control for the battery charging

Conventionally, two separate control loops are required for this operation, as shown in Fig.3. 17. The proposed controller offers certain specific advantages that increase the suitability of the proposed converter as an on-board battery charger, which are listed as follows:

a) Stage 1 of the converter can be controlled using only a single control signal. This is because the upper switches, S_1 and S_3 of each leg, are operated as a diode, whereas the bottom switches, S_4 and S_6, continue to turn on and off according to the direction of the power supply. It is possible because, despite the gating signal, the switch will not be turned on unless a positive drain-source voltage appears across it. During the positive half of the supply, only switch S_4 turns on, and the body diode of S_6 conducts. During the negative half, only S_6 and the body diode of S_4 conduct.

b) As the second stage, the resonant converter (HB-LLC) operates at fixed duty, an additional control loop is eliminated, simplifying the converter's mathematical modeling.

c) The number of sensing parameters is reduced. Thus, the need for an additional voltage sensor to sense the DC link voltage is eliminated.

The control operation is done by reducing the requirement of the sensing elements and creating a single control loop, as shown in Fig.3. 18.

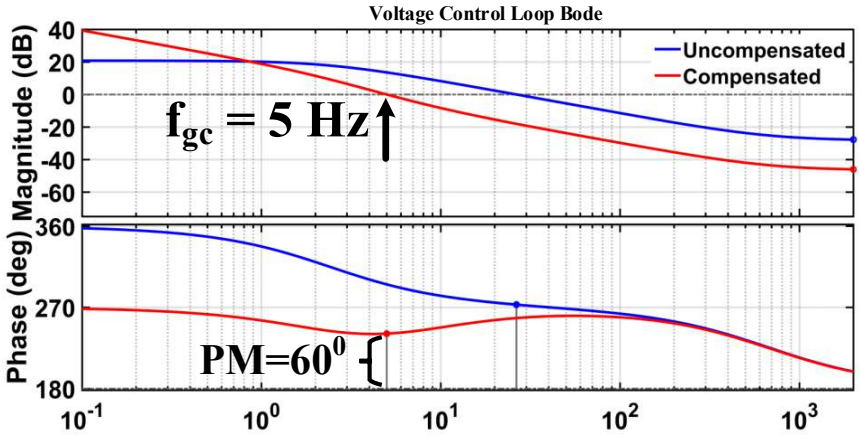

Fig.3. 20 Bode plot of voltage loop control.

3.3.2.2 Voltage control loop

The small signal analysis is conducted and determines the $\frac{\hat{v}_{bat}}{\hat{\imath}_{in}}$ transfer function as given in Eq. 3.6. The control parameters Kp (Proportional gain) and Ki (integral factor) are determined with the help of these transfer function parameters. To filter out the low-order harmonic from the output voltage and maintain stability, the voltage compensator should have a narrow bandwidth and pass the Nyquist criteria for stability.

The bandwidth of this transfer function is 5 Hz at a phase margin of 60^0 and GM of 46.7 dB at infinity, which can easily filter out the double-line power frequency but affects the

dynamic operation. This is compensated by a digital controller and improves the faster dynamic compensator during load jumps for better output regulation.

The bode plot of the voltage control loop is given in Fig.3. 20. The output of the PI_1 controller is normalized by the input voltage loop gain, which makes the controller independent of the input voltage range. The output of the voltage compensator is fed into the multiplier, and the other two inputs are multiplied as well. 1st is the rectified value of the instantaneous input voltage, and 2nd is the inverse of the square value of the input RMS voltage.

$$\begin{bmatrix} \dot{\hat{i}}_L \\ \dot{V}_{DC} \end{bmatrix} = \begin{bmatrix} 0 & \frac{-(1-D)}{L_T} \\ \frac{-(1-D)}{C_{DC}} & \frac{1}{RC_{DC}} \end{bmatrix} \begin{bmatrix} \hat{i}_L \\ V_{DC} \end{bmatrix} + \begin{bmatrix} \frac{1}{L_T} \\ 0 \end{bmatrix} V_{in} + \begin{bmatrix} \frac{V_{DC}}{L_T} \\ \frac{-i_L}{C_{DC}} \end{bmatrix} D \tag{3.5}$$

$$\left. \frac{V_{DC}}{\hat{i}_{in}} \right|_{V_{in}=0} = \frac{\frac{(1-D)}{L_T C_{DC}} V_{DC} - S\frac{i_L}{C_{DC}}}{S\frac{V_{DC}}{L_T} + \frac{2\times V_{DC}}{RL_T C_{DC}}} \tag{3.6}$$

$$V_{bat} = Mg_{n*}\frac{1}{n} * \frac{V_{DC}}{2}$$

Where: $\hat{V}_{DC}$ (DC-link voltage), $\hat{\imath}_{in}$ (input current), $\hat{V}_{in}$ (input voltage), C_{DC} (DC-link capacitor), L_T ($Ls + L_{BLDC}$), i_L (source inductor current), R (Load resistance), Mg_n (intermediate converter gain =1 for (nominal frequency)), n (Transformer turn ratio)

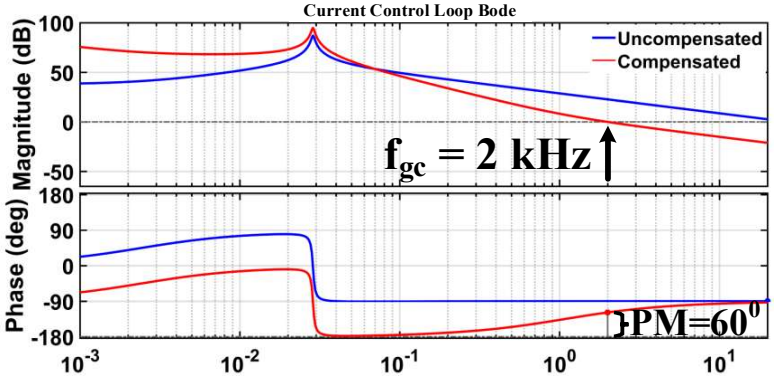

Fig.3. 21 Bode plot of the current control loop.

3.3.2.3 Current control loop

The small signal analysis is conducted and determines the $\frac{\hat{\imath}_{in}}{\hat{D}}$ control loop transfer function as given in Eq. 3.7. This transfer function determines the control parameters kp and ki, which maintain the unity power factor.

The bandwidth of the transfer function is kept at 10 % or below the switching frequency, and here it is 2 kHz at a phase margin of 60^0 and GM of infinity, as shown in Fig.3. 21. The output of the controller generated the pulse for switches S4 and S6, which maintains the power factor at the source terminal and charges the battery with the CC-CV charging technique.

$$\left.\frac{\hat{i}_{in}}{D}\right|_{V_{in}=0} = \frac{\frac{SV_{DC}}{L_T} + \frac{2\times V_{DC}}{RL_TC_{DC}}}{S^2 + \frac{S}{RC_{DC}} + \frac{(1-D)^2}{L_TC_{DC}}} \tag{3.7}$$

3.4 Comparative analysis

To highlight the advantages of the proposed converter, it is compared in terms of performance and cost with the existing literature, and the results are discussed in the following subsections.

3.4.1 Performance analysis with similar prior work

The comparative analysis with similar prior work is shown in Table 3. 2. In [101], a converter with 16 switches has two interleaved cells with two full-bridge rectifiers to charge the battery. However, two interleaved cells with two transformers increase the control complexity of the converter. In [102], a single-stage on-board charger with a reduced switch count is presented. However, in both [101][102] an additional inverter is required for driving a motor. In [103], a coupled magnetic-based integrated isolated onboard charger is used to charge the battery and drive the motor. However, for charging and motoring operations, the number of switch counts is increased. In [104], for the same operation, the number of switch counts is decreased. However, galvanic isolation is missing in the onboard charger, which is essential for preventing the current from entering from the grid to the vehicle. Further, it does not generate the multioutput for charging the main battery and an additional 12 V battery, which is used for low-power auxiliaries. In [105], the onboard charger is integrated to charge the main battery and an additional 12 V battery for the low-power auxiliaries. However, an additional inverter is required for motor drives.

The proposed multimode onboard power converter drives the BLDC motor with a high-PWM low-ON switching technique, generates the regulated output voltages for the power support of the EV cabin, and provides galvanic isolation during single-phase charging.

Table 3. 2 Comparative analysis with similar prior work

L.N.	No. of Stages	Galvanic isolation	Need of Inverter for motor drive	No. of MOSF-ETS	No. of diodes	Additional switches	Total No. of Switches	Multi output	Requirement of additional 12 V Battery
[101]	2	Yes	Yes	4	12	0	16	No	Yes
[102]	1	Yes	Yes	10	4	0	14	No	Yes
[103]	2	No	No	20	0	4	24	No	Yes
[104]	2	No	No	10	4	1	15	No	Yes
[105]	1	No	Yes	10	4	2	16	No	Yes
Proposed	2	Yes	No	8	3	7	18	Yes	No

Table 3. 3 Cost comparative analysis

S.No.	Components	Conventional System			Proposed System	
		Motoring Mode	Charging Mode	Total (USD)	Components	Total (USD)
1	Switches, Diode	6	6,2	12x21+2x5.2	8,3	8x21+3x5.22
2	Heat sink	1	1	2x20	1	20
3.	Gate Driver &Accessories	6	6	12x3.34+10	8	8x3.34 + 7
4.	PCB	1	1	2x62.5	1	62.5
5.	DC-DC converters	1		47	0	0
6.	12 V (AGM) Battery	1		249	0	0
7.	Speed control converter	1		5	0	0
8	Relay	0	0	0	7	7x20
Total Cost (in $)				**782**		**441**

3.4.2 Cost Comparative Analysis

The comparative cost analysis of the proposed converter with the conventional converter is shown in Table 3. 2. The details of the components are: switch (IXFH18N100Q3), diode (RURG8060), heat sink (1960012091T00S), gate driver (FOD3184), PCB (FR4 epoxy glass), DC-DC converter, 12 V Absorbent glass mat battery (Duralast Platinum), speed control converter for the BLDC motor, and relay (V23076-A3001-C132). The total cost of the conventional system is USD 782, and the proposed system is USD 441. The total cost saving from the proposed system is 341 USD.

3.4.3 Power density of the proposed system

A photograph of the laboratory-scale prototype is shown in Fig.3. 22. The volume of the experimental prototype of the proposed topology is measured to be 7.8 dm^3.

The power density of a converter is defined as [106]

$$= \frac{Rated\ power\ output\ by\ the\ converter}{Total\ volume\ of\ the\ converter}$$

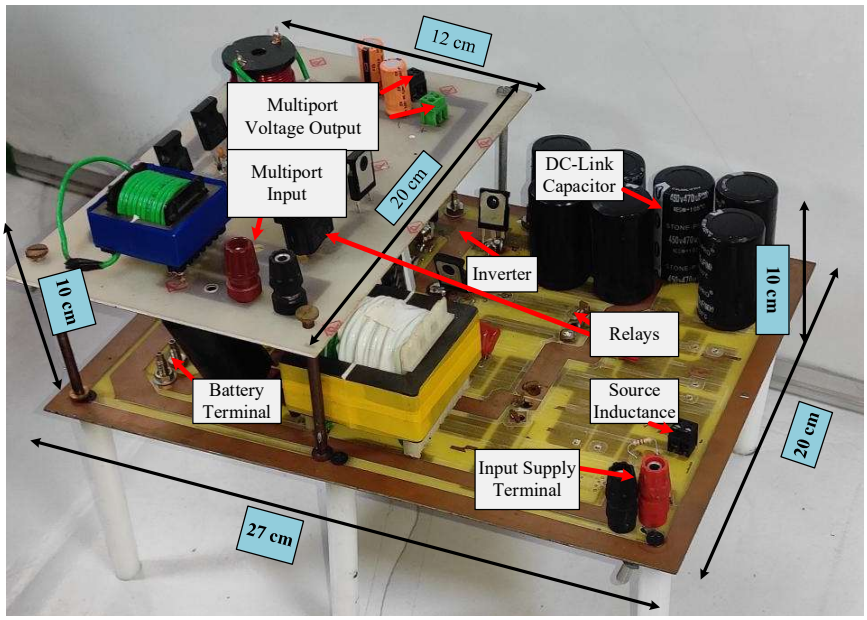

Fig.3. 22 Pictorial representation of the proposed converter.

The rated output power of the proposed converter in its charging and motoring modes is 500 W and 1000 W, respectively. The power density of the inverter in [107] is 70 kW/liter, and the power density of the proposed converter used as an inverter is 128 kW/liter. The power density of the single-phase AC/DC converter in [106] is 35 kW/ dm^3, and the power density of the proposed converter at charging is 64 kW/ dm^3. The proposed topology achieves a significant improvement in power density by 45.31 % for motoring mode and 46 % for charging mode, respectively, as compared to existing counterparts.

Table 3. 4 Specification of the proposed converter

Specifications	Values	Specifications	Values
$V_{battery}$	48 V	L_A	0.8 mH
V_{01}	72 V	L_B	0.6 mH
V_{02}	12 V	C_{DC_Link}	3 mF
V_{ac_input}	120 V	C_{bat}	470 uf
Power	550 W	C_{01}	470 uf
f_S (FEC)	20 kHz	C_{02}	100 uF
f_S (LLC)	19.29 kHz	BLDC Motor	4P,1000 W
Lr	35 uH	Cr	2uF

3.5 Experimental validation

The pictorial representation of the experimental prototype is shown in Fig.3. 22 The specification and the component rating of the converter are given in Table 3. 4. Their results are described in the sequence of multifunction with multioutput, and V2V charging.

3.5.1 Motoring mode

In the motoring mode, a 48 V, 1000 W, four-pole BLDC is driven by a 48 V battery, along with generating the regulated auxiliary voltages of 12 V and 72 V, respectively.

3.5.1.1 Hall effect position sensing

For running the BLDC motor, the exact position of the rotor is traced by the hall-effect sensors H1, H2, and H3, as shown in Fig.3. 23. The hall-effect sensor has 180^0 conduction and 120^0 parts from each other [108]. The operation of the motor according to these hall-effect sensors can be understood by the Table 3. 1.

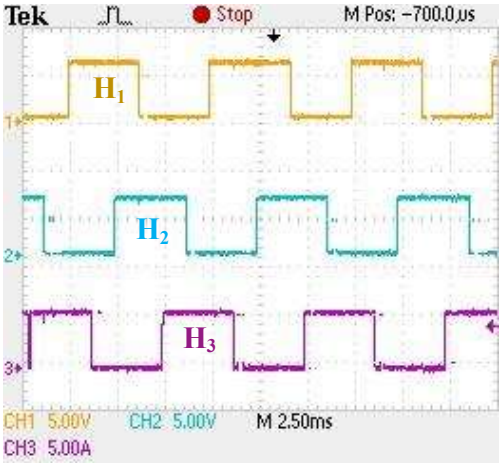

Fig.3. 23 The output waveform of hall-effect position sensors.

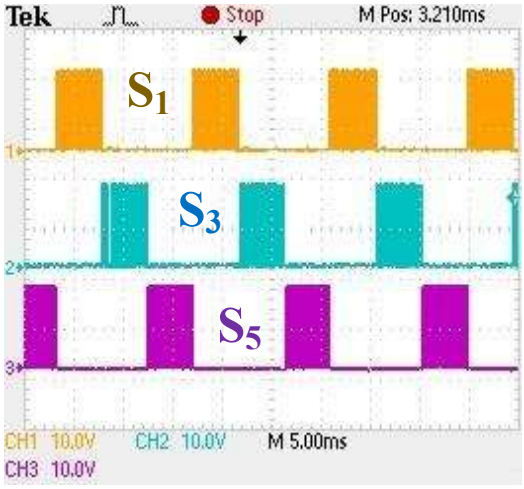

(a)

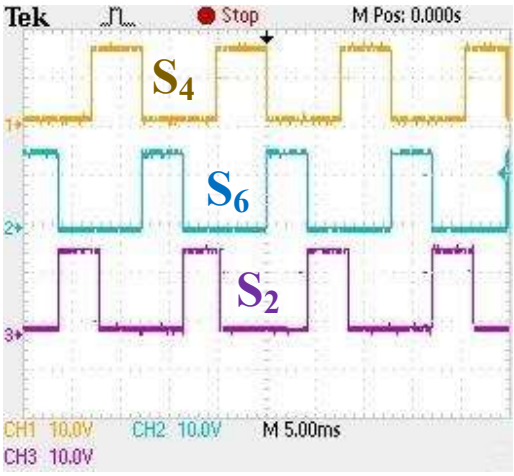

(b)

Fig.3. 24 HPLS for BLDC motor drive, (a) upper leg, and (b) lower leg of the inverter.

3.5.1.2 High-PWM Low-ON switching (HPLS) scheme

According to the rotor position, the inverter is triggered with high-PWM low-ON switching, as shown in Fig.3. 24. The speed of the motor is controlled by varying the pulse width of the upper leg switches S_1, S_3, and S_5, and the lower switches S_2, S_4, and S_6 are turned ON for their respective time interval. A zoomed view of the switching sequence during the speed control is shown in Fig.3. 25 (a) and (b). By decreasing the width (W_1>W_2), the speed of the motor is decreased. In the BLDC, the motor speed is linearly dependent upon the applied voltage.

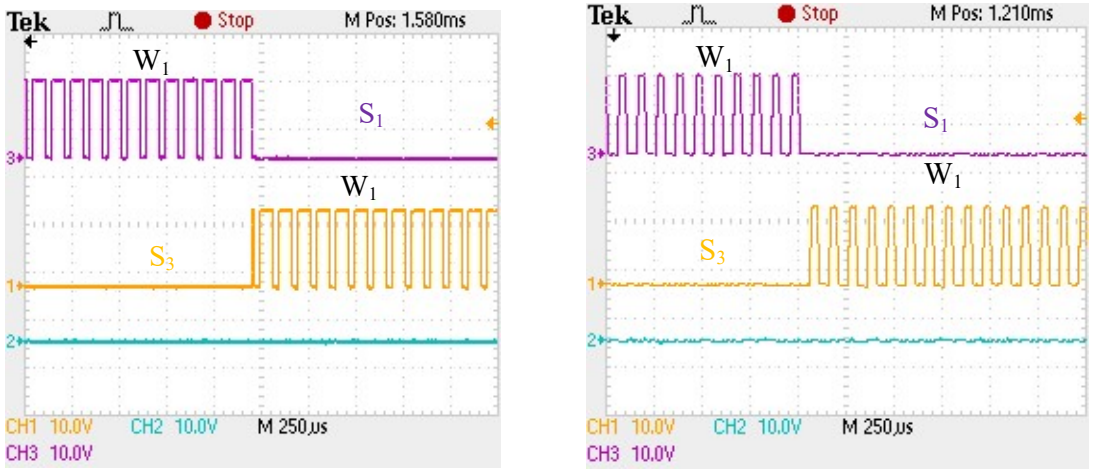

(a) (b)

Fig.3. 25 Switching sequence of switches S_1, S_3 at (a) speed 2100 rpm, (b) 1900 rpm.

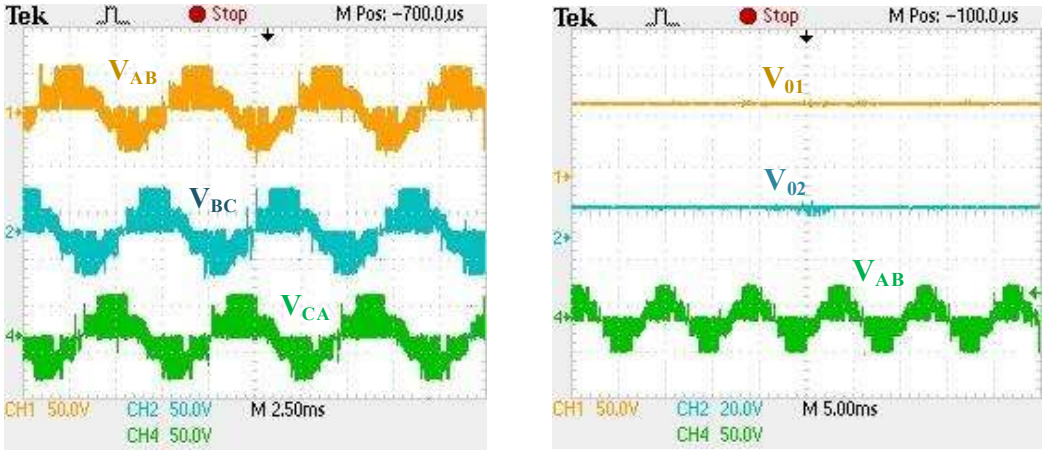

(a) (b)

Fig.3. 26 (a) Inverter line voltage in motoring operation and (b) auxiliary output voltages and line voltage V_{AB}.

3.5.1.3 Inverter line voltage with auxiliary output voltages

Inverter line voltages V_{AB}, $V_{BC,}$ and V_{CA} are 120^0 phase shift during motor mode operation, as shown in Fig.3. 26(a). In motoring mode operation, the regulated auxiliary voltages of 12 V and 72 V are generated to power the EV cabin as shown in Fig.3. 26(b).

3.5.1.4 Commutation torque ripple reduction

Phase-a current and the drain-to-source voltage across switch S_1 are shown in Fig.3. 27. It may be clearly observed that for the switch current $I'_{A,}$ the commutation current ripple is significantly reduced. In a similar manner, the commutation current ripple in the inverter switches S_6 and S_2 is also reduced by the proposed HPLS technique.

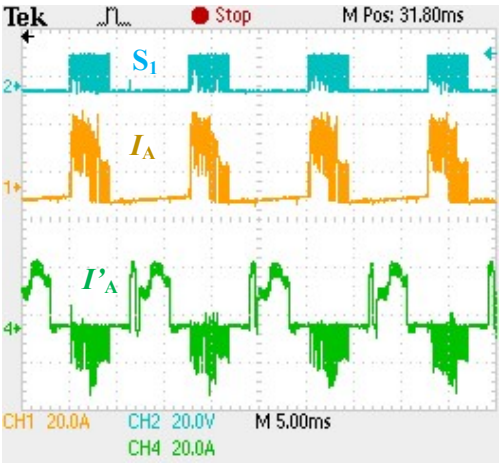

Fig.3. 27 Experimental validation of the proposed HPLS scheme demonstrating elimination of commutation current ripple from current I′A.

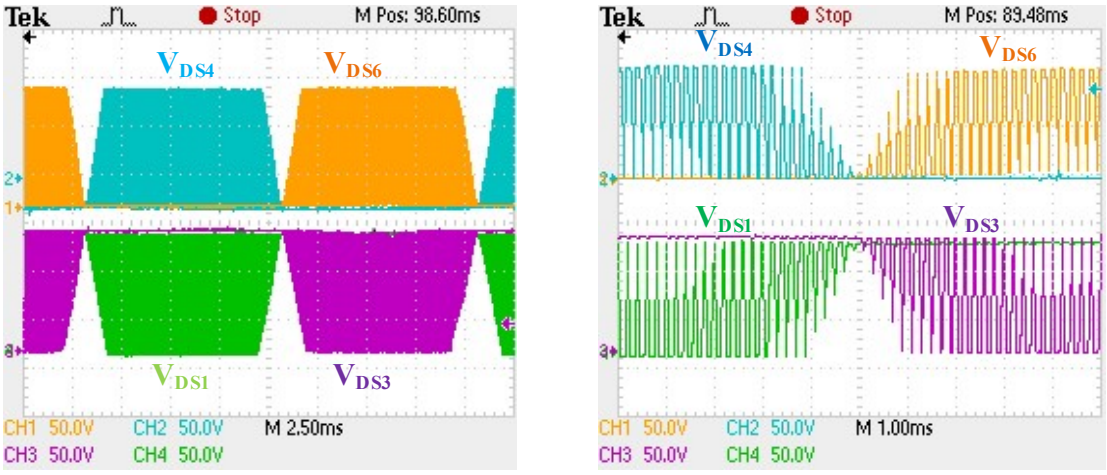

(a) (b)

Fig.3. 28 (a) The switching sequence of the boost PFC in charging mode and its zoomed view are shown in (b).

3.5.2 Charging mode

3.5.2.1 Switching sequence of FEC

The proposed power converter maintains the unity power factor at the source terminal and charges the battery using the CC-CV charging technique. It is achieved by switching the sequence S_4 and S_6, and the voltage across the switches is given in Fig.3. 28(a) and its zoomed view is given in Fig.3. 28 (b).

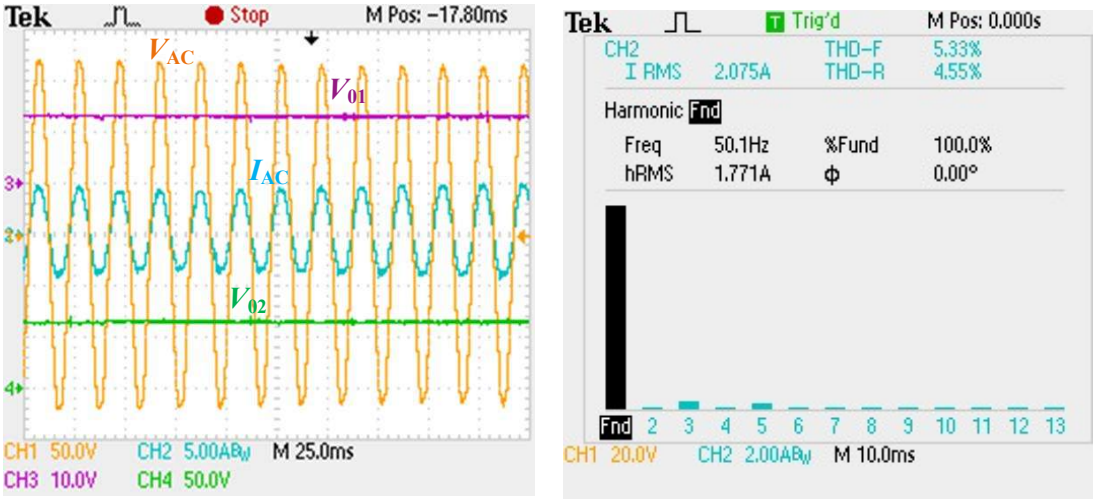

(a) **(b)**

Fig.3. 29 (a) Unity power factor with auxiliary power supply V_{01} and V_{02} and (b) THD spectrum of the source current

3.5.2.2 PFC of the proposed converter

The PFC with auxiliary' power supplies is given in Fig.3. 29 (a). V_{AC} and I_{AC} represent the input voltage and current, and V_{01} and V_{02} represent the regulated auxiliary voltages generated to power support the EV cabin. Further, the THD spectrum of the source current is given in Fig.3. 29 (b). The total harmonic distortion as a percentage of the RMS (THD-R) value of the waveform is 4.33%, and the total THD-F is a percentage of the fundamental rms value of the waveform is 5.33%.

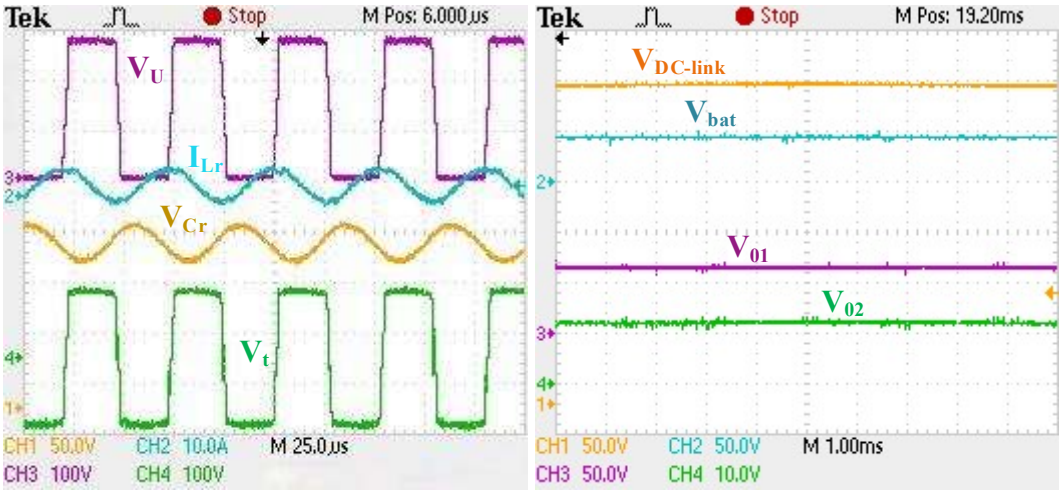

(a) (b)

Fig.3. 30 (a) HB-LLC operation, and (b) available outputs during the charging operation.

3.5.2.3 Properties of the HB-LLC

The HB-LLC provides zero voltage switching (ZVS), and its constant gain at normalized frequency removes the requirement for additional sensors, which simplifies the control operation. For ZVS operation, when the switch is ON, the current should flow through the body diode of the switch, which can be seen in Fig.3. 30(a).

The available output voltages during charging are shown in Fig.3. 30 (b), where $V_{DC\text{-}LINK}$, Vbat, V_{01}, and V_{02} represent the DC-link voltage, battery voltage, high-power auxiliary voltage, and low-power auxiliary voltage, respectively.

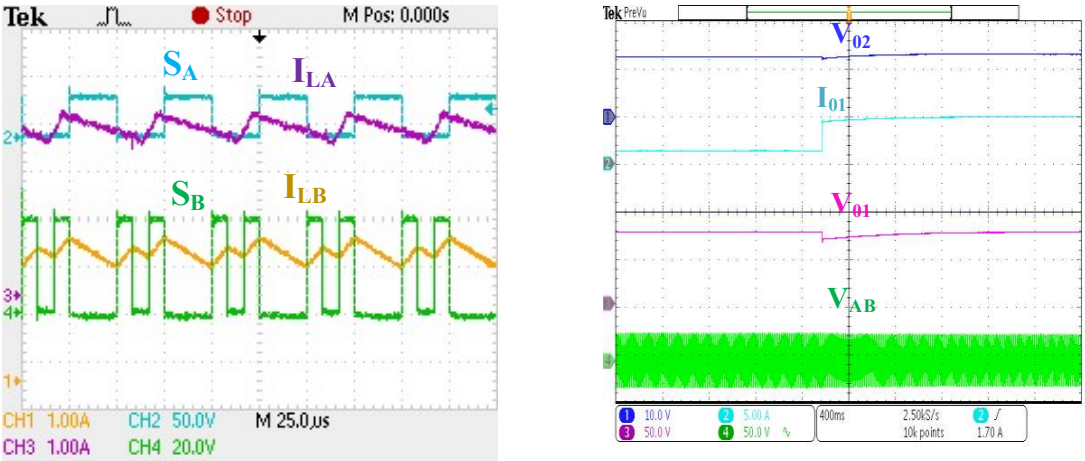

(a) (b)

Fig.3. 31 S_A, S_B switching with inductor L_A and L_B current profile I_{LA} and I_{LB}, respectively, (b) stable voltage regulation in motoring mode during load dynamic.

3.5.3 Auxiliary power supply with V2V charging

The proposed power converter generates auxiliary power supplies to cater to the power demand of the EV cabin in charging and motoring modes. The switches S_A and S_B are switching, and according to that switching, the inductors' L_A and L_B current profiles, I_{LA} and I_{LB} are shown in Fig.3. 31(a).

The stable voltage regulation in motoring mode during a load transient applied at the high-power auxiliary as a resistive load is shown in Fig.3. 31(b). where I_{01} and V_{01} represent high-power auxiliary current and voltage, respectively. V_{AB} and V_{02} represent the line voltage of the inverter and the low-power auxiliary voltages of the converter.

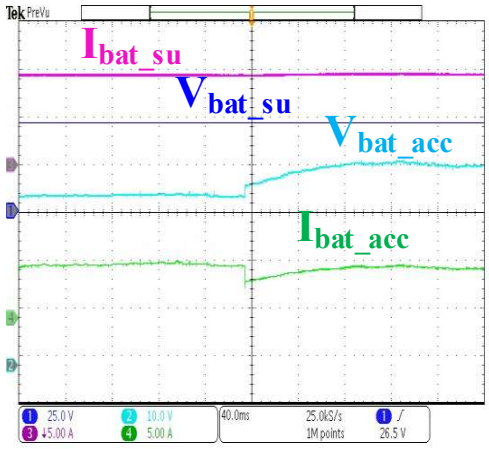

Fig.3. 32 Voltage and current profile of an energy supplier vehicle's battery, and current and voltage profile of an energy acceptor vehicle at a resistive load in place of the battery.

During V2V charging, the supplier vehicle powers the low-power and high-power auxiliary, along with the energy acceptor vehicle. A load dynamic is applied in the energy acceptor vehicle as a resistive load, and the constant current changing technique is shown in Fig.3. 32. Where $I_{bat\text{-}su}$ and $V_{bat\text{-}su}$ represent the current and voltage profile of the energy supplier vehicles, and the $V_{bat\text{-}acc}$ and $I_{bat\text{-}acc}$ represent the current and voltage of the energy acceptor vehicle.

3.6 Conclusion

This chapter presents a BLDC motor drive with an adaptable multifunction power processor having multimode operations. In multifunction, the proposed converter performs charging as well as motoring operations and generates auxiliary power supplies for the EV cabin. Further, in its multimode properties, vehicle-to-vehicle charging is provided by

restructuring itself with three changeover switches. The proposed converter charges the 48 V battery from the single-phase 120 V, 50 Hz power supply and generates 12 V and 72 V to the power supply of the EV cabin. The proposed converter is restructured as an inverter with an auxiliary power supply converter that drives the BLDC motor and supplies the auxiliary power supply to the EV cabin. The charging mode is tested at 500 W, where the proposed converter charges the 48 V, 36 Ah battery and powers the auxiliaries of the EV cabin by a unified control loop. Furthermore, the proposed converter is restructured to efficiently drive the 4-pole 1000 W BLDC motor with a High-PWM Low-ON switching technique while simultaneously supplying power to the auxiliary systems of the EV cabin. The auxiliary power supplies generate the regulated voltage of 12 V and 72 V. The 12 V output eliminated the requirement for an additional 12 V battery and its charger, and 72 V decreases the current demand by the high-power auxiliaries by the 48 V main battery. The 72V regulated output is used as a connection point for V2V energy exchange in the energy supplier and acceptor vehicles. The proposed power processor's comparative analysis and cost analysis with similar prior work are listed in a tabular form. Further, the power density of the proposed power processor is calculated and compared with similar previous work.

The work carried out in this chapter has some limitations: 1) Seven changeover switches are used for operating mode selection. 2) Three changeover switches are used to restructure the circuit of the energy supplier and acceptor vehicle for V2V charging.

In the next chapter, the integrated circuit architecture is modified with a reduced switch count from 18 to 14. Further, only three switches are used for mode selection. In the modified on-board power processor, vehicle-to-vehicle (V2V) charging is achieved by directly connecting the proposed power processors of both vehicles. Also, eliminating the need for changeover switches in the circuit configuration during V2V charging. Only six active switches perform V2V charging and provide mobile charging, which removes range anxiety in the consumer's mind.